Numerical Study on Wave Propagation in a Row of Topologically Interlocked Tetrahedra

Tanner Ballance[1] and Thomas Siegmund[1*]

[1]School of Mechanical Engineering, Purdue University, 585 Purdue Mall, West Lafayette, 47907, Indiana, USA.

*Corresponding author(s). E-mail(s): siegmund@purdue.edu;
Contributing authors: tballanc@purdue.edu;

Abstract

This study is concerned with the mechanics of wave propagation in a type of architectured, granular, material system. Specifically, we investigate wave propagation in a topologically interlocked material (TIM) system. TIM systems are assemblies of polyhedrons in which individual polyhedrons cannot be removed from the assembly without complete disassembly due to the geometric interlocking of the polyhedrons. The study employs an explicit finite element code to compute phase velocities, amplitude distributions, and wave patterns in a linear assembly of topologically interlocking tetrahedra. Tetrahedra are considered fully 3D linear elastic bodies interacting with neighboring tetrahedra by contact and friction. We demonstrate the propagation of a solitary wave along the row of tetrahedra. The velocity of the wave is found to be independent of amplitude for an idealized contact, but dependent of amplitude for a realistic asperity contact. In the absence of friction and for contact the wave velocity is determined to be approximately 50% the material wave speed, but increases in the presence of friction to about 80% of the material wave speed. We attribute the wave velocity to wave guiding as set by the geometry of the tetrahedra assembly geometry and a rocking motion of tetrahedra on an axis perpendicular to the wave propagation direction. The degree to which such rocking motion occurs is affected by friction.

Keywords: Architectured Granular Material Systems; Wave Propagation; Wave Front; Guided Waves

1 Introduction

Wave Propagation in material systems created by the assembly of granular unit elements has attracted considerable interest. The systems under consideration are commonly composed of spheres, ellipsoids, and cylinders [1, 2] and are either arranged in a single row or in a planar array [3, 4]. The complexity of these systems is limited by the available spherical shapes. Commonly, investigations include rows or arrays of a single type of geometry [5–7] but systems comprised of multiple spherical shapes have also been of interest[8–10].

The systems containing typical curved elements such as spheres have nonlinear dynamic behavior that arises from the nonlinear (Hertz) contact interaction between bodies. Specifically, the propagation of nonlinear solitary waves is a dynamic behavior that has been well documented in these systems [1, 3]. Wave propagation in a row of such spherical unit elements can be reduced to a one-dimensional problem, while wave propagation in an array of such units is a two-dimensional planar problem as contact is either confined to a line or plane, respectively.

Topologically Interlocked Material (TIM) systems are also assemblies of granular unit elements. Here, the building blocks are polyhedrons with the TIM systems constructed such that no building block can be removed from the assembly without the disassembly of the system overall [11, 12]. These systems can be assembled from all identical unit elements or be built from a structured mix of several different unit elements [11, 13, 14].

It has been demonstrated that, for quasi-static loading, load transfer in a planar array of interlocking polyhedron building blocks is non-planar and can be described by a force-network approach [15–17]. Unlike assemblies of spherical units [18], TIM systems can bear loads transversely to the assembly plane with a gradual failure response of the TIM system even if building blocks are made of brittle solids [19]. This response characteristic persists under impact loading and can make TIM systems attractive for potential applications in the mitigation of dynamic loading events [20]. However, the mechanics of wave propagation in polyhedron-based TIM systems has yet to be investigated.

Recent work on the mechanics of blocky material systems, in the context of fragmented geomaterials, relates to the present work [21–23]. These studies indicate the potential for significant nonlinear wave propagation responses in blocky material systems due to the bi-linear nature of the open-closed contact [22], as well as the rotational degree of freedom in the system [21, 23]. Nevertheless, it is not evident how key effects observed in the wave propagation in systems of spheres (such as the solitary wave propagation and the impact velocity of wave speed) would translate to the problem of wave propagation in an assembly of polyhedrons. Consequently, the objective of this study is to expand the knowledge on wave behavior in assemblies made of discrete polyhedral unit elements. We advance this field by conducting a computational study of the wave propagation in a single row assembly composed of topologically interlocked tetrahedra.

This study addresses the following research questions:

- What is the effective wave speed in a row of topologically interlocked tetrahedra, and how does this wave speed compare to that of the corresponding monolithic solid?
- What is the wave propagation mode in a row of topologically interlocked tetrahedra, and how do the normal and tangential contact properties of the system affect wave propagation?

The specific objectives of this study are

- To use finite element analysis to obtain wave speeds for a row of topologically interlocked tetrahedra in dependence of the dilatational wave speed of the solid and the material system architecture.
- To execute such computations under consideration of friction effects, as well as under consideration of idealized and realistic (exponential) contact pressure-overclosure relationships.
- To define equivalent quasi-1D models for the analysis of overall unidirectional in-plane wave propagation in a topologically interlocked row of tetrahedra.

2 Methods

2.1 Geometry

Figure 1 depicts a planar array of interlocking tetrahedra, the key geometric template. This configuration is the densest packing of tetrahedra in 2D [24]. A tetrahedron is locked in place by its nearest neighbors and cannot be removed from the assembly without the disassembly of the overall system. One representative row of tetrahedra is highlighted in Fig. 1. For the present study, only that row of tetrahedra is of concern. Instead of considering the full planar assembly, Fig. 1, the representative row of tetrahedra, Fig. 2(a), is embedded into a rigid guiding frame, Fig. 2(b), positioning the individual tetrahedra relative to each other and representing the remainder of the planar assembly.

The analysis is concerned with the propagation of a wave along the row of tetrahedra when an initial velocity is applied to the first tetrahedra (the striker). The geometry of the guiding frame is obtained by fusing two (adjacent) rows of interlocking tetrahedra such that the lateral contact surface positions match that of the planar tetrahedra assembly, Fig. 1. To further define the geometry of the model, a section view of the system is provided in Fig. 2(c).

The length of the row, L, spans the midplanes of the tetrahedra:

$$L = a_0 \frac{N}{2}. \qquad (1)$$

where N is the number of tetrahedra within the span of the row and a_0 is the tetrahedra edge length. The edge to edge distance of the unit tetrahedra

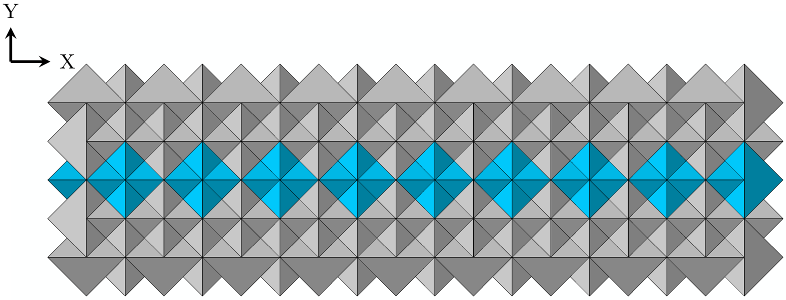

Fig. 1 A planar array of interlocking tetrahedra. Assembly of 5 × 18 unit elements. The highlighted row of tetrahedra is constrained by the rows above and below it.

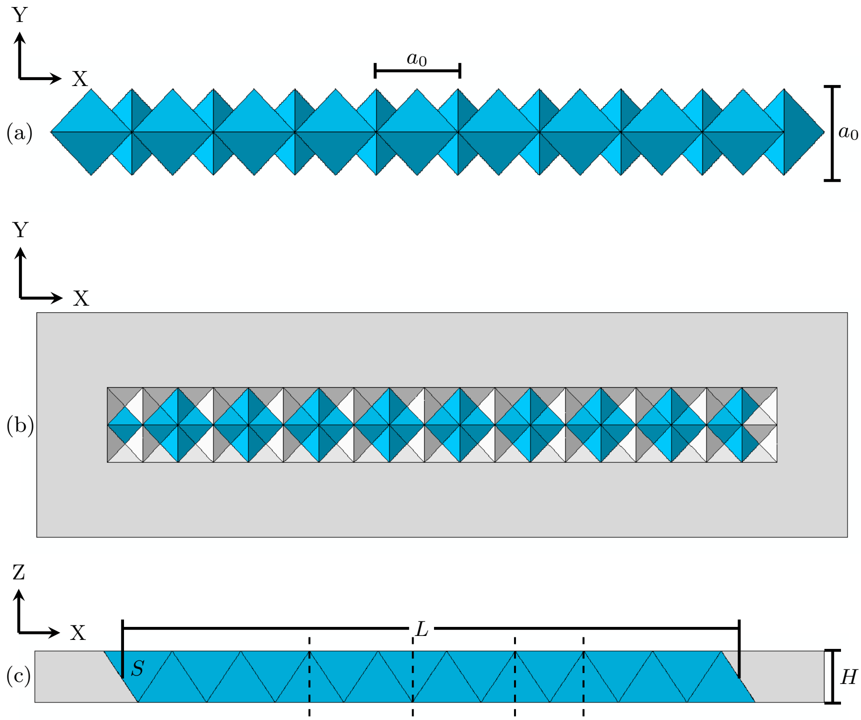

Fig. 2 The tetrahedra row model. (a) The row of topologically interlocking tetrahedra, (b) The row of topologically interlocking tetrahedra constrained by the complementary guiding frame, (c) Cross-section of the row of topologically interlocking tetrahedra of (b), S indicates the striker, dashed lines indicate the integrated output sections used for analysis (tetrahedra #6, #9, #12, #14).

defines the model height, H:

$$H = a_0 \frac{\sqrt{2}}{2}. \tag{2}$$

2.2 Model Definition

Tetrahedra are considered to be linear elastic solids with modulus of elasticity, E, Poisson's ratio, ν, and density, ρ. The wave speed along a 1D bar is $c_d = \sqrt{E/\rho}$. We consider $E = 193$ GPa, $\nu = 0.3$, and $\rho = 8000$ kg/m^3, so $c_d = 4911.7$ m/s. The model is an assembly of 18 tetrahedra, of which the first tetrahedron is the striker (S), 2. Model geometry is set by defining the tetrahedron edge length, $a_0 = 25$ mm. With the given parameters, a model characteristic time, t^*, is determined by the time it takes for a wave to traverse a_0 through the chosen material, *i.e.* $t^* = 5.090$ μs.

A velocity boundary condition, $V_x = V_0 \sin^3(\pi t/t_p)$, is applied to the entire body of the first tetrahedra, the striker, with V_0 being the reference input velocity and t_p being the impact duration. The reference input velocity is considered over the range of 0.1 to 1.0 m/s, and $t_p = 20$ μs. A wave propagating through a monolithic solid would travel a distance of $4a_0$ during t_p.

Two types of contact interaction between tetrahedra are considered. One approach being a linear contact-pressure, p, overclosure, h, approach and other other being an exponential overclosure approach. A linear contact interaction is used to represent an idealized contact condition between two flat surfaces:

$$p(h) = \begin{cases} 0 & h \le 0 \\ Kh & h > 0 \end{cases} \tag{3}$$

A linear contact with limited overclosure values is imposed by using a numerically large value for the contact stiffness $K = 1000E/l_0$, with l_0 being unit length.

Real surfaces, even if parallel to each other, do not follow the linear, idealized, $p - h$ response as there exists some form of surface roughness. In [25] a contact model capturing the interaction between real (rough) but nominally parallel surfaces is suggested. An exponential "softened" $p - h$ relationship is defined:

$$p(h) = \begin{cases} 0 & h \le -d \\ \frac{p^0}{e-1}\left[\left(\frac{h}{d}+1\right)\left(e^{\frac{h}{d}+1}-1\right)\right] & h > -d \end{cases} \tag{4}$$

where d is an initial contact definition and p^0 is a characteristic contact pressure value. This investigation considers two pairs of parameter values in Eq. 4: $p^0 = 1.0$ kPa, $d = 0.01$ μm (Exp-A) and $p^0 = 1.0$ kPa, $d = 0.0175$ μm (Exp-B). Figure 3 depicts both the linear and the exponential contact laws.

The tangential interaction between tetrahedra follows the Coulomb friction model. A reference set of computations considers a frictionless, $\mu = 0.0$, condition. Further computations consider a coefficient of friction $0 \le \mu \le 0.5$.

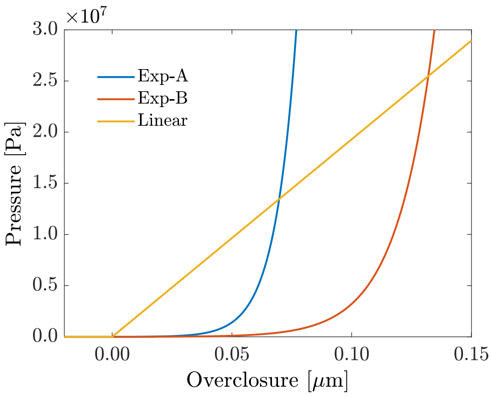

Fig. 3 Contact interactions. The linear pressure-overclosure relationship and the two exponential pressure-overclosure relationships considered.

The guiding frame is considered to be a rigid body and is fixed in space. It is constructed to match the dimension H, possesses a width of $3a_0$ and a length of $(N+2)a_0$. The normal contact interaction between tetrahedra and the frame is always identical to that considered between tetrahedra. The tangential interaction between the frame and the tetrahedra row assumes $\mu = 0.0$ in all cases.

2.3 Analysis

The computational model is realized and executed with the ABAQUS/Explicit finite element code. All tetrahedra possess the same finite element mesh. The element type used is a 10 node three-dimensional tetrahedral element with modified implementation for accurate contact computation (C3D10M). The element size is $a_0/20$ such that the distance $c_d t_p$ is sufficiently discretized. The numerical response of the model was assessed by a mesh sensitivity study, Appendix A. The mesh for the frame component employs the same element type and mesh density. However, the frame is ascribed a rigid body constraint. A surface-to-surface contact interaction is used. This contact interaction uses a main-secondary surface definition in which the main surface is allowed to penetrate the secondary surface. In a tetrahedron-to-tetrahedron contact pair, the main surface is defined with an outward normal in x^+. Based on the element size of $a_0/20$ a stable increment for the model would need to be smaller than 0.255 μs. The as-executed code determines an initial time increment of 0.0197 μs, yet most of the computation is executed with a time increment of 0.031 μs.

Wave propagation is captured by defining integrated output sections at chosen tetrahedron. An integrated output section is a defined surface used for variables that are computed from integration over that surface. Therefore, an integrated output section resultant force response, $F_S(t)$, is computed from the normal stress at the tetrahedron section (x^+, at the midplane of a tetrahedron) over the section area. The effective wave speed, $\hat{c}$, is determined by obtaining the wave travel time between two defined integrated output sections. Specifically, the two sections used are those of tetrahedron #6 and #14, Fig. 2, located at a distance of $(14-6)/2a_0 = 4a_0$. A threshold of $0.5[F_S(t)/F_S^0]$ is used to determine the arrival times of the wave at the output sections. $F_S^0 = \max(F_S(t))$ is the peak value of the integrated output section resultant force $F_S(t)$.

The integrated section output for tetrahedron #9 is used for visualization of the wave pulse. Wave propagation is further visualized by contour plots of the minimum (most compressive) principal stress, σ^P_{min} on the $x-z$ section of the row of tetrahedra, Fig. 2(c).

Contact pressure values on the surface of this tetrahedron are investigated as representative examples and are compared to pressure values computed for quasi-static conditions. For such analysis two tetrahedra are employed, one tetrahedron is held fixed and with a prescribed displacement applied to the opposing tetrahedron. The spatial distribution of contact pressure is independent of the applied load. The contact response in obtained from the quasi-static analysis is compared to the dynamics analysis to understand the transient evolution of the contact pressure.

Lastly, the pitch of the tetrahedra is computed. Pitch, θ, is defined as the angle between the tetrahedra edges initially aligned in x with respect to the x^+-axis:

$$\sin(\theta) = \left(\frac{u_z^2 - u_z^1}{a_0}\right). \tag{5}$$

Here, u_z^2 and u_z^1 are the z-axis displacements of the two vertices that are axially aligned of the tetrahedron edge that is parallel to the axis of the model row length. Pitch is evaluated for tetrahedron #9.

2.4 Model Verification

A verification of the computational model is performed on monolithic and segmented prismatic bars. The monolithic prismatic bar model is a uniform solid bar. It possesses the same width, a_0, and height, $H = a_0\sqrt{2}/2$, as an individual tetrahedron, and is of length equal to the row of tetrahedra. A corresponding segmented prismatic bar consists of 18 unit blocks of lengths equivalent to $a_0/2$. The overall length of the segmented bar is then equivalent to the length of the other models. In the segmented prismatic bar, the linear contact model and the exponential contact model are considered. No friction is present, $\mu = 0$. Building blocks are constrained to move in the direction of wave propagation only. Material properties are identical to those used in the simulation of the tetrahedra row. Both the monolithic and segmented bars are discretized with the C3D10M tetrahedral elements with element size of $a_0/20$. Finite element models are solved with the code ABAQUS/Explicit.

For the monolithic prismatic bar, the computation provides an effective wave speed close to c_d, specifically, $\hat{c}/c_d = 0.98$. Wave speed is also found to be independent of the reference input velocity. The effective wave speed for the monolithic prismatic bar, $\hat{c}$, is obtained from the wave travel time between

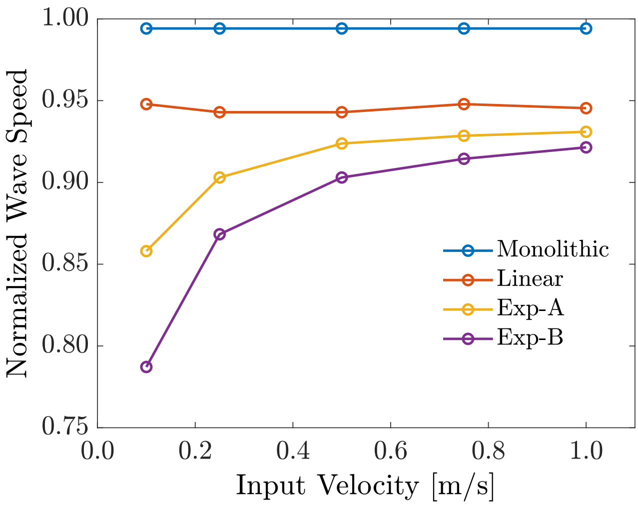

Fig. 4 Model verification. Normalized wave speeds, $\hat{c}/c_d$ computed for the monolithic prismatic bar and the segmented prismatic bar. Linear and exponential contact models.

sections at $L/3$ and $2L/3$. Results of the simulations are summarized in Fig. 4, as $\hat{c}$ normalized by c_d. For the segmented prismatic bar the effective wave speed, $\hat{c}$, is determined using the wave travel time from and the distance traveled between the integrated output sections of blocks # 6 and #14 using a 50% threshold on the force pulse.For the segmented prismatic bar and the idealized linear contact, the prismatic segmented bar model predicts $\hat{c}$ again independent of the reference input velocity. The linear contact introduces additional compliance into the model, and $\hat{c}/c_d = 0.94$. For models with the exponential contact law, the effective wave speed is found to be non-linearly dependent on the impact velocity with $\hat{c}$ reaching that of the linear contact at the highest level of impact velocity.

3 Results

3.1 Row of Tetrahedra: Linear Contact Model with $\mu = 0.0$

We first consider an idealized reference model, a linear contact in the absence of friction. Figure 5(a) shows the integrated output section resultant force, $F_S(t)$, for tetrahedron #9. The peak force value is found as dependent on reference input velocity V_0, yet the wave shape is independent of V_0. This is demonstrated in Fig. 5(b) by depicting $F_S(t)/F_S^0$ and the finding of a unique pulse shape. Fig. 5(c) demonstrates that force peak values are linearly dependent on the reference input velocity V_0.

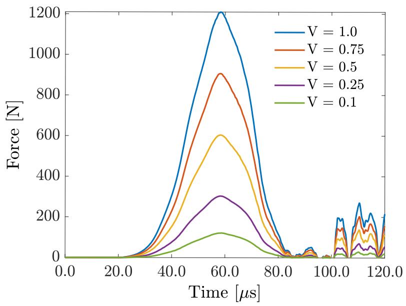

(a)

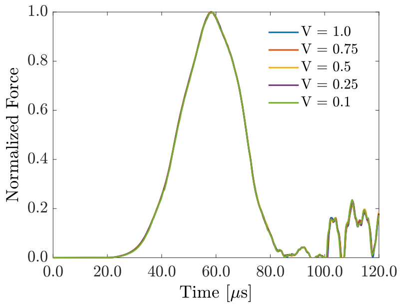

(b)

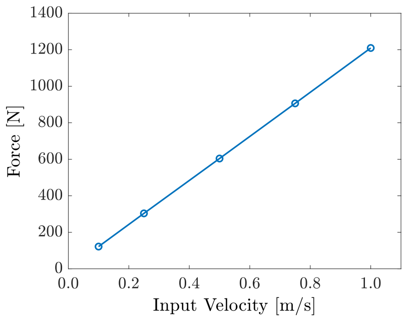

(c)

Fig. 5 Linear contact with $\mu = 0.0$. (a) Integrated output section resultant force in tetrahedron #9 for selected values of the reference input velocity V_0 [m/s]. (b) Peak value normalized integrated output section resultant forces in tetrahedron #9 for selected values of the reference input velocity V_0 [m/s]. (c) Peak values of the integrated output section resultant force calculated in tetrahedron #9 *vs.* reference input velocity V_0.

Figure 6(a) depicts the resultant force, $F_S(t)$, for tetrahedra #6, #9, #12, and #14, and shows the wave propagate through the system. As the wave traverses the space between tetrahedra #6 and #9, a minor transient response following the impact gives way to the fully developed wave by tetrahedron #12. Force data is normalized by the peak values of the respective integrated output section, Fig. 6(b). Circle symbols indicate the respective thresholds used to obtain wave travel times between these sections. Using this information and the distance between sections of #6 and #14, the effective wave speed, c_d, is determined. We find the effective wave speed, $\hat{c}/c_d = 0.47$, to be independent of the reference input velocity, V_0, Fig. 6(c). Wave speeds calculated between the different pairing of tetrahedra lead to only minor changes of the predicted value. For instance, the pairing of tetrahedra #9 and #12 resulted in $\hat{c}/c_d = 0.48$, while for #6 and #9 $\hat{c}/c_d = 0.46$. Considering all permutations of tetrahedra pairings, an average value for the wave speed is $\hat{c}/c_d = 0.47$. In the subsequent, tetrahedra #6 and #14 are used to assess wave speeds. Based on the findings of the wave propagating with a near constant shape and near

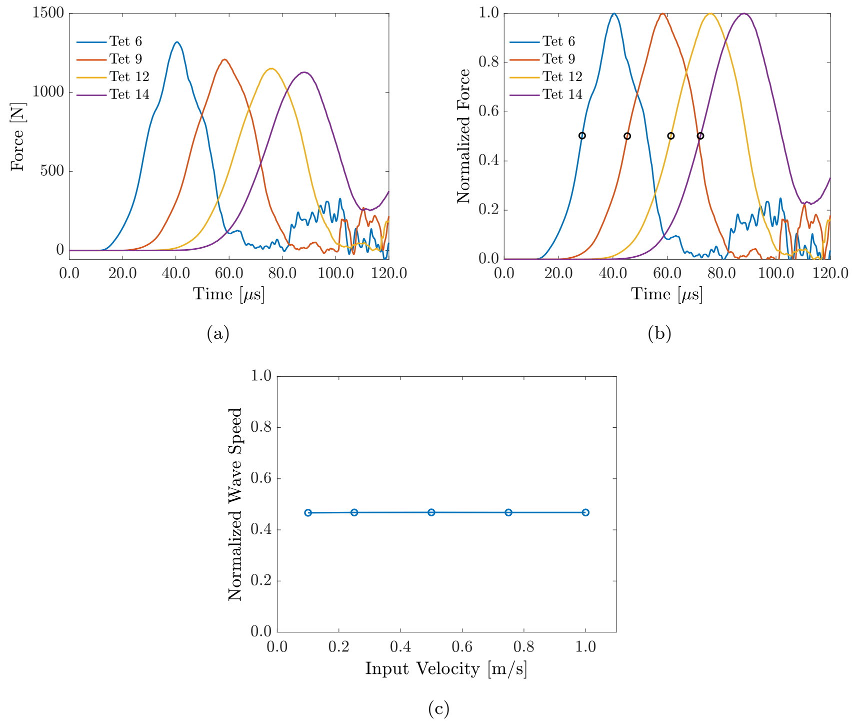

Fig. 6 Linear contact model with $\mu = 0.0$. (a) Integrated output section resultant force in tetrahedra #6, #9, #12, and #14, $V_0 = 1$ m/s. (b) Peak value normalized integrated output section resultant force in tetrahedra #6, #9, #12, and #14 are used to calculate effective wave speed (the 50% threshold of the force pulse is indicated), $V_0 = 1$ m/s. (c) Normalized effective wave speed ($\hat{c}/c_d$) *vs.* the reference input velocity V_0.

constant amplitude, the wave propagation along the row of tetrahedra fulfills the definition of a solitary wave.

In general, a mesh with an element size of $a_0/20$ is used for analysis. A brief sensitivity study on element sizes was performed to determine an adequate element size. This was done by computing the differences between meshes of different seed sizes for peak values of the integrated output sections forces and wave speeds. The sensitivity between a seed size of $a_0/20$ and a seed size of $a_0/40$ was found to be small enough to conclude that the seed size of $a_0/20$ is adequate for capturing the wave behavior in the models for all cases of input velocity and coefficient of friction.

Contour plots of the minimum (most compressive) principal stress in the cross-section bisecting the assembly along its length provide insight into the propagation of the wave, Fig. 7. As a wave packet travels along the row of tetrahedra (in x^+), it also moves transversely, in z^+ and z^-. Figures 8(a)-(d) depict the evolution of the contact pressure on tetrahedron #9 as the wave traverses this unit. The wave crosses surfaces in contact perpendicularly but

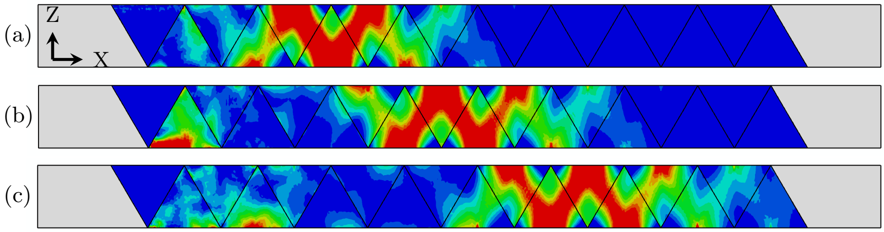

Fig. 7 Visualization of wave propagation through the tetrahedra assembly, linear contact model, $\mu = 0.0$, $V_0 = 1.0$ m/s. Contour plots of the minimum (most compressive) principal stress, σ^P_{min}, in the tetrahedra row cross section: (a) t =40 μs, (b) t = 60 μs, and (c) t =80 μs. Contour colors: blue ($\sigma^P_{min} > 0$ Pa) to red ($\sigma^P_{min} < 15 \times 10^6$ Pa).

also rolls across the surfaces. This rolling behavior is apparent in the transient development of the spatial distribution of contact pressure on the surface. Figure 8(e) depicts the contact pressure distribution between two tetrahedra under static loading. In that case the contact pressure distribution is symmetric about the tetrahedra midplane. In the dynamic case, as the pressure pulse traverses the surface, the contact pressure first possesses the location of maximum pressure above the midplane, Fig. 8(a-b), then the maximum moves to the midplane, Fig. 8(c), and later is found to be located below the midplane of the tetrahedron, Fig. 8(d).

We associate the transients in the spatial distribution of the contact pressure in a case where slip between surfaces is possible with the pitch of the tetrahedra. Figure 9 depicts the computed pitch angle for tetrahedron #9. The tetrahedron initially possesses its upper edge aligned with the $x-$axis. As the wave propagates along the row of tetrahedra, this initial alignment is disturbed and the pitch angle deviates from zero. The pitch angle becomes negative, i.e. the tetrahedron rotates in the clockwise direction around the y-axis. The negative pitch is the associated with the asymmetry in the contact pressure distribution in Fig. 8(a). Then, pitch returns to zero and the contact pressure distribution becomes symmetric, Fig. 8(b-c). Subsequently, pitch becomes positive, i.e. the tetrahedron rotates in the counter-clockwise direction around the y-axis. The positive pitch is associated with the asymmetry in the contact pressure distribution in Fig. 8(d).

3.2 Row of Tetrahedra, Linear Contact Model with $\mu > 0$

Contact surfaces between tetrahedra are not perpendicular to the overall wave propagation direction, i.e. the axis of assembly. Therefore, it is of interest to investigate the effect of friction on wave propagation.

Figure 10(a) depicts the normalized resultant section forces for tetrahedron #9 and several values of μ. The results indicate that an increase in the coefficient of friction affects the propagation of solitary waves in the interlocking tetrahedra row. For $\mu = 0.5$ the width of the wave pulse is about half of that for $\mu = 0.0$, and a gradual narrowing with the increase in μ is observed.

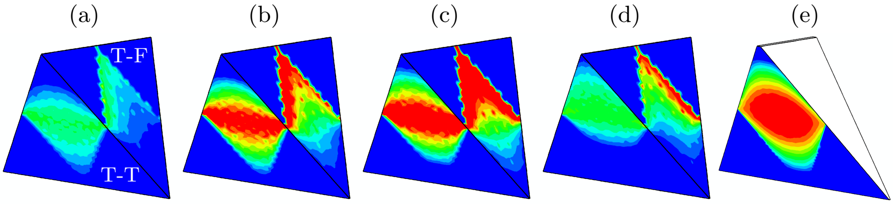

Fig. 8 Linear contact model, $\mu = 0.0$, $V_0 = 1.0$ m/s. Distribution of computed contact pressure, p, tetrahedron #9: (a) $t = 40$ μs, (b) $t = 50$ μs, (c) $t = 60$ μs, (d) $t = 70$ μs, and (e) pressure distribution for linear contact model with $\mu = 0.0$ under static load. T-T: tetrahedron-to-tetrahedron contact surface, T-F: tetrahedron-to-frame contact surface. Contour colors: blue (no contact) to red ($p > 15 \times 10^6$ Pa).

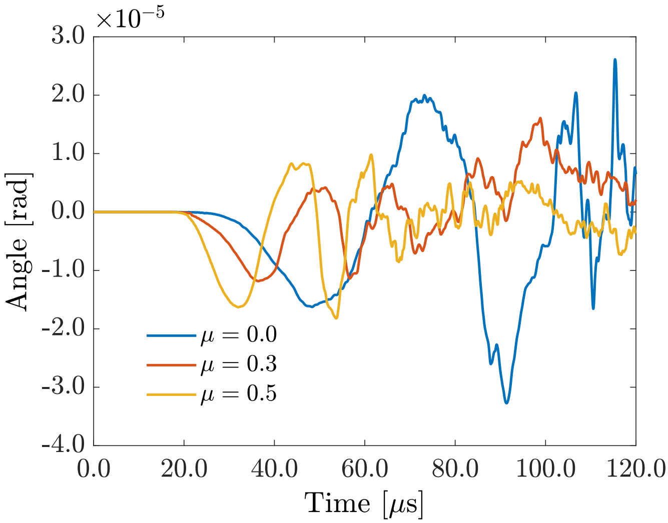

Fig. 9 Pitch angle for tetrahedron #9, $V_0 = 1.0$ m/s. Linear contact with $\mu = 0.0$ compared to cases $\mu = 0.3, \mu = 0.5$.

Figure 10(b) also shows that the resultant force magnitude has a nonlinear dependence on μ, with the case of $\mu = 0.5$ exhibiting a force magnitude around 1.5 times the peak value of the $\mu = 0.0$ model. The maximum dynamic force is found to be nonlinear dependent on μ for a given velocity. Figure 10(c) shows the dependence between wave speed and input velocity for all chosen values of μ. An increase in the coefficient of friction increases the speed but the wave speed remains independent of input velocity at each value of μ. Figure. 10(d) depicts the dependence of the wave speed on μ for $V_0 = 1.0$ m/s.

The contour plots of the minimum (most compressive) principal stress for $\mu = 0.5$ are given in Fig. 11. As observed with the frictionless model, the axial wave propagation is associated with significant transverse wave propagation. While the force pulse wave is more narrow with friction, the width of the high compressive stress wave is larger with friction than in the absence of friction.

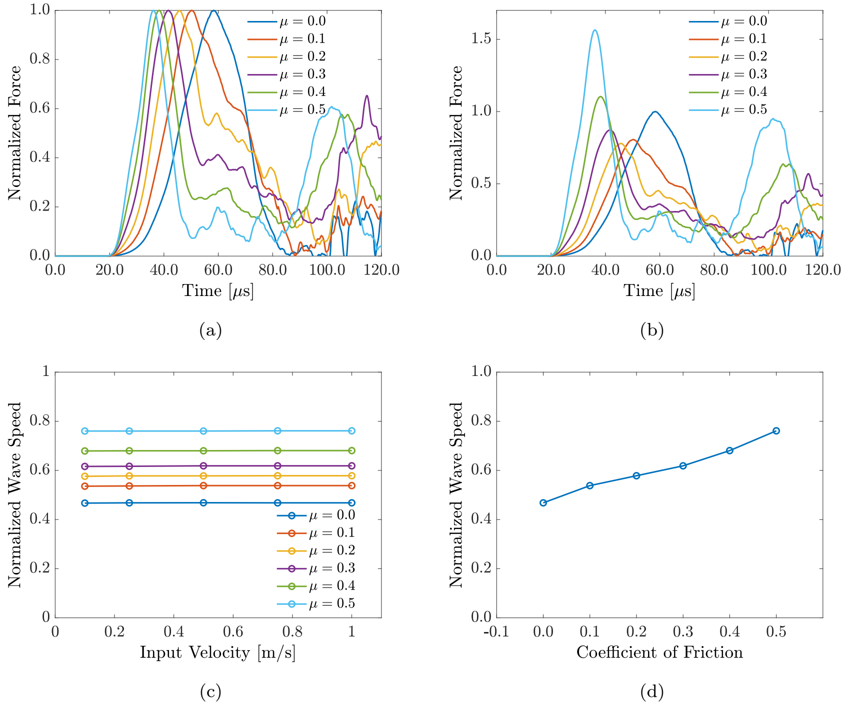

Fig. 10 Linear contact model with $\mu \leq 0$. (a) Peak value normalized integrated output section resultant forces, $V_0 = 1.0$ m/s (tetrahedron #9) for a range of friction values, (b) Integrated output section resultant forces normalized to the peak force value for $\mu = 0$, $V_0 = 1.0$ m/s (tetrahedron #9), (c) Normalized effective wave speed ($\hat{c}/c_d$) *vs.* the reference input velocity V_0, (d) Normalized effective wave speed ($\hat{c}/c_d$) *vs.* coefficient of friction, $V_0 = 1.0$ m/s.

The broader distribution of load within the tetrahedra is also visible from the contact pressure distribution, Fig. 12 for tetrahedron #9. Also, the contact pressure and contact area remain largely centered at the tetrahedron midplane throughout. Considering Fig. 9, friction is associated with a reduction of the pitch angle such that tetrahedron edges remain dominantly aligned with the reference configuration.

3.3 Exponential Contact Model with $\mu = 0.0$

It is of interest to incorporate surface roughness into numerical models to better approximate real materials. Nonlinearity is introduced with the exponential contact model of Eq. 4. Figure 13(a) depicts the wave pulse for the two exponential contact models with the wave pulse for the linear contact model. The rise of the wave pulse is affected by the contact model, but the fall of the wave is not. The rise of the wave depends depends on the parameter, d, used to distinguish the two different exponential contact models. Figure 13(b) shows the effective wave speed in dependence of the input velocity for the three model.

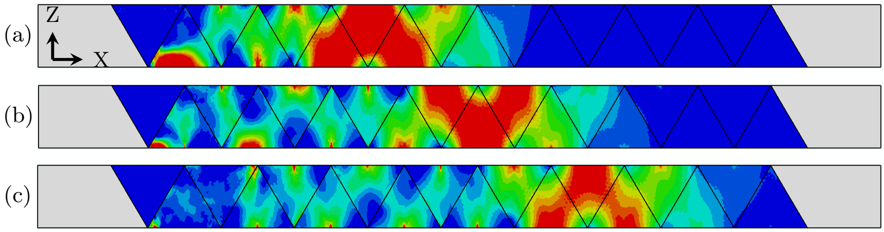

Fig. 11 Visualization of wave propagation through the tetrahedra assembly, linear contact model, $\mu = 0.5$, $V_0 = 1.0$ m/s. Contour plots of the minimum (most compressive) principal stress, σ^P_{min} in the tetrahedra row cross section: (a) $t = 30$ μs, (b) $t = 40$ μs, and (c) $t = 50$ μs. Contour colors: blue ($\sigma^P_{min} > 0$ Pa) to red ($\sigma^P_{min} < 15 \times 10^6$ Pa).

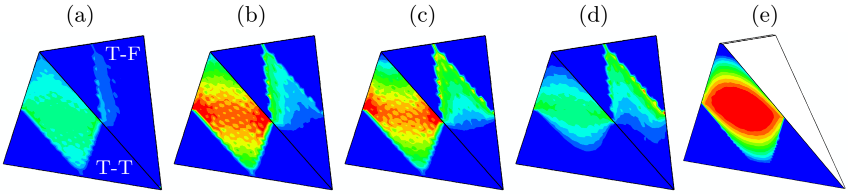

Fig. 12 Linear contact model, $\mu = 0.5$, $V_0 = 1.0$ m/s. Distribution of computed contact pressure, p, tetrahedron #9: (a) $t = 26$ μs, (b) $t = 32$ μs, (c) $t = 38$ μs, (d) $t = 44$ μs, and (e) pressure distribution for linear contact model with $\mu = 0.5$ under static load. T-T: tetrahedron-to-tetrahedron contact surface, T-F: tetrahedron-to-frame contact surface. Contour colors: blue (no contact) to red ($p > 15 \times 10^6$ Pa).

For the two exponential models there is a nonlinear dependence of the wave speed on input velocity, V_0, but at high input velocities, the predicted wave speeds converge towards those for the linear contact model.

The contour plots of the minimum (most compressive) principal stress are shown in Fig. 14 for Exp-A. The spatial distribution of σ^P_{min} for the model with the exponential contact model is found to be overall similar to that for the linear and frictionless case, Fig. 7. Yet at the same time, wave peak for the exponential model is wider than that for the linear model, indicating that the presence of surface asperity can affect wave width. Transient contact pressure distributions for tetrahedron #9 for the exponential model (Exp-A) are shown in Fig. 15. Again, the spatial distribution of contact pressure changes as the wave propagation progresses. Initially, Fig. 15(a) contact pressure is present below the unit block midplane, Fig. 15(b-c), and finally above the midplane, Fig. 15(d). Here, the degree of asymmetry in the contact pressure distribution is the most significant for all cases considered. Figure 16 shows the evolving pitch angle of tetrahedron #9 for the exponential models in comparison to the computation with the linear contact model. The initially soft contact in the exponential contact model delays the onset of the formation of a non-zero pitch angle, i.e. increases the clockwise rotation of the tetrahedron. The

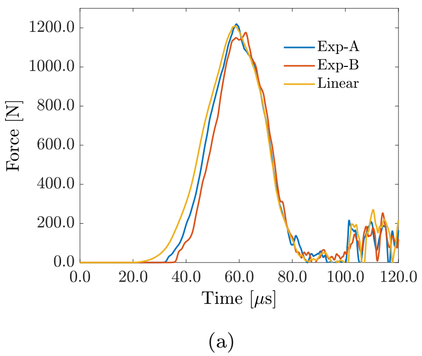

Fig. 13 Exponential contact model with $\mu = 0.0$. (a) Integrated output section resultant force, $V_0 = 1.0$ m/s (tetrahedron #9), (b) Normalized effective wave speeds ($\hat{c}/c_d$) *vs.* the reference input velocity $V_0 = 0.0$ for all contact models.

backward rotation at the later stages of the contact transient is less affected by the contact model.

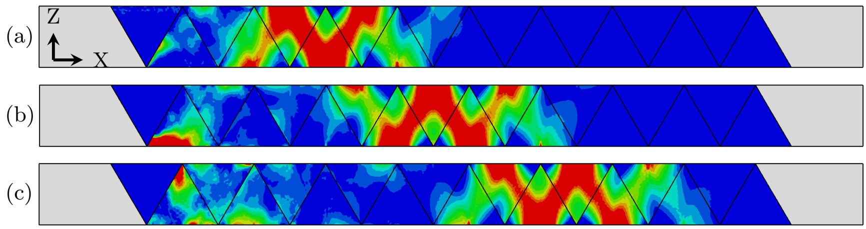

Fig. 14 Visualization of wave propagation through the tetrahedra assembly, exponential contact model (Exp-A), $\mu = 0.0$, $V_0 = 1.0$ m/s. Contour plots of the minimum (most compressive) principal stress, σ^P_{min} in the tetrahedra row cross section: (a) $t = 40$ μs, (b) $t = 60$ μs, and (c) $t = 80$ μs. Contour colors: blue ($\sigma^P_{min} > 0$ Pa) to red ($\sigma^P_{min} < 15 \times 10^6$ Pa).

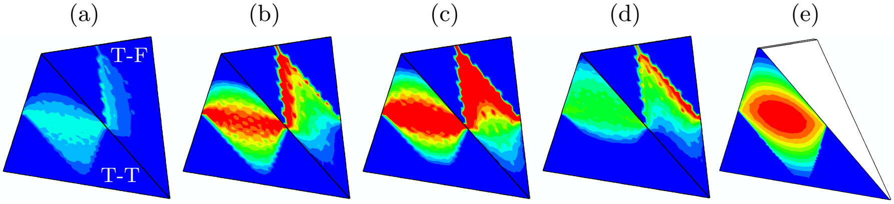

Fig. 15 Exponential contact model (EXP-A), $\mu = 0.0$, $V_0 = 1.0$ m/s. Distribution of computed contact pressure, p, tetrahedron #9: (a) $t = 40$ μs, (b) $t = 50$ μs, (c) $t = 60$ μs, (d) $t = 70$ μs, and (e) pressure distribution for Exp-A with $\mu = 0.0$ under static load. T-T: tetrahedron-to-tetrahedron contact surface, T-F: tetrahedron-to-frame contact surface. Contour colors: blue (no contact) to red ($p > 15 \times 10^6$ Pa).

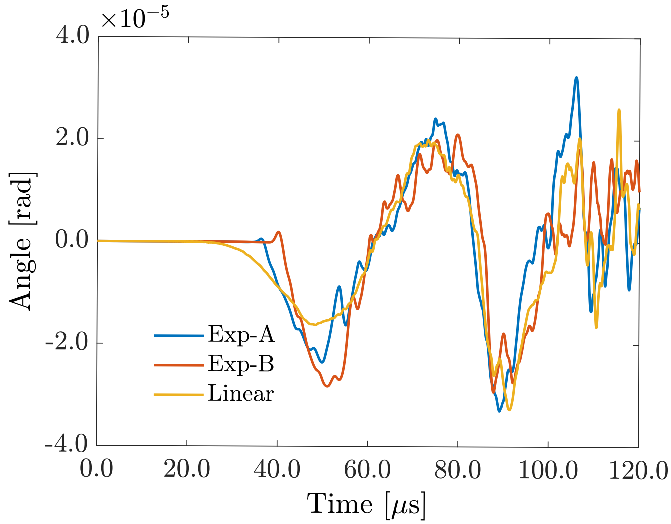

Fig. 16 Axial pitch between in-line corners of tetrahedron #9 for different exponential contacts Pitch angle for tetrahedron #9, $V_0 = 1.0$ m/s. Exponential contact models and the linear contact model, $\mu = 0.0$.

4 Discussion

This study uses numerical simulations with an explicit finite element analysis to obtain insights into wave propagation behavior for a row of geometrically interlocked tetrahedra. Idealized, linear contact conditions and frictionless interactions are considered as a baseline. Contact interaction models approximating real surfaces with asperities and friction are considered as well.

In the prismatic bar segmented into prismatic blocks with edges aligned with the assembly axis and interacting by contact, then the effective wave speed in such segmented systems is only minimally altered by the presence of the linear contact interaction. In the row of the topologically interlocked tetrahedra and considering linear contact the predicted effective wave speeds are found to be $\hat{c}/c_d \approx 0.5$ and independent of the magnitude of the impact velocity. When all the tetrahedra are fused to their respective neighbours, i.e. in a monolithic body with an effective geometry identical to that of the row of tetrahedra, the wave speed is calculated as $\hat{c}/c_d = 0.91$. This value is much larger than that found for the row of tetrahedra and close to that of the prismatic bar (monolithic or segmented). Consequently, the geometry of the system segmentation must play a central role in the wave propagation along the row of individual tetrahedra.

The information provided by the contours of principal stresses and the contact pressure, indicate the path of the wave in the system. Figure 7(a) depicts the effective path for the propagation of the wave under the idealized conditions (linear contact and frictionless).

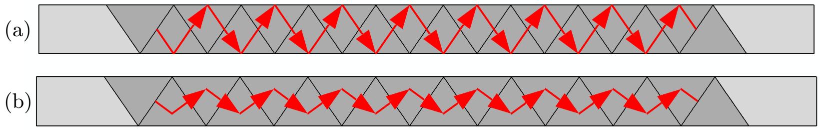

Fig. 17 Effective path for wave propagation in the row of tetrahedra. (a) Frictionless conditions, (b) No-slip (high friction) conditions.

The effective wave path possesses a significant transverse component, Fig. 7. At each instance, the load transfer across the contact is in the normal direction, but the location of the active contact patch evolves with time Fig. 8 as quantified by the pitch angle Fig. 9. Then, based on these insights, an equivalent quasi-1D model for the wave propagation in the topologically interlocked row of tetrahedra under idealized interaction conditions (linear frictionless contact) can be established. This leads to the abstracted wave path depicted in Fig. 17(a). This path is defined by the wave reflection locations at the mid point of the tetrahedra edges aligned with the x-axis. The effective length $\hat{L}^{\mu=0}$ of the path of the wave is:

$$\hat{L}^{\mu=0} = a_0 N = 2L \tag{6}$$

This model leads to an effective wave speed of $\hat{c}^{\mu=0}/c_d = 0.5$.

We find that friction increases the wave speed. In the presence of significant friction, the effective wave path continues to possess a transverse component, Fig. 11. Yet, in the presence of friction, the location of the active contact patch minimally evolves with time Fig. 12, as quantified by the pitch angle Fig. 9. Consequently, we define the effective wave path to cross orthogonal to the contact surfaces at the midsection of the tetrahedra. The respective wave path is depicted in Fig. 17(b). This effective length, $\hat{L}^{\mu=0.5}$, of the path of the wave is:

$$\hat{L}^{\mu=0.5} = \frac{\sqrt{6}}{4} a_0 N = \frac{\sqrt{6}}{2} L \tag{7}$$

This model leads to an effective wave speed of $\hat{c}^{\mu}/c_d = 0.81$.

The wave speeds found through the detailed analysis of the computation are in close agreement those obtained with effective wave path models, Fig. 17. For the case of linear contact and with $\mu = 0.0$, Fig. 6(b), the FE model results in a computed wave speed of $\hat{c}/c_d = 0.47$. Considering linear contact and $\mu = 0.5$, Fig. 10(c), the FE model results in a computed wave speed of $\hat{c}/c_d = 0.76$. The differences between the wave speeds as determined from the full finite element model and the effective path model arise from a combination of the geometric envelope and the compliance introduced by the contact stiffness. The effect of the contact stiffness on wave speed is evidenced in Fig. 4, where a loss in wave speed is incurred upon segmenting a monolithic prismatic bar. Likewise, the geometric envelope itself is associated with a reduction in the wave speed even for the monolithic cases.

The concept of the effective path length can be further explored.

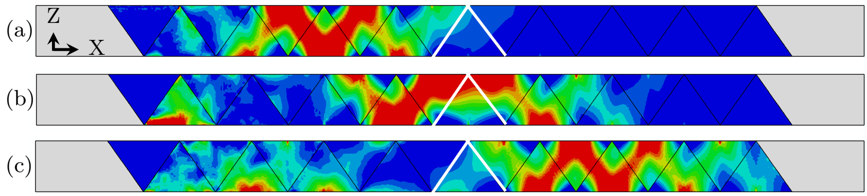

Fig. 18 Visualization of wave propagation through the partially fused tetrahedra assembly, linear contact model, $\mu = 0.0$, $V_0 = 1.0$ m/s. The white bars highlight the surfaces between tetrahedra #9 to #11 that have been fused together. Contour plots of the minimum (most compressive) principal stress, σ^P_{min} in the tetrahedra row cross section: (a) t =40 μs, (b) t = 60 μs, and (c) t =80 μs. Contour colors: blue ($\sigma^P_{min} > 0$ Pa) to red ($\sigma^P_{min} < 15 \times 10^6$ Pa).

First, in the FE simulations we considered the effect of magnitude of the coefficient of friction. The effective path model can be used in this case. For intermediate values of the coefficient of friction, the linear combination of the two effective wave propagation paths can be used to establish the effective path length.

Furthermore, instead of considering an assembly consisting of all individual tetrahedra, one can construct the assembly where a select few tetrahedra have been fused together. The specific computation discussed here considered tetrahedra #9 to #11 fused to each other, Fig. 2(c). The computation with the FE model leads to an effective wave speed of $\hat{c}/c_d = 0.52$. This wave speed is also predicted based on an effective path motivated by Fig. 18, where the wave takes a path along the top edge of the assembly where tetrahedra #9 to #11 are fused, rather than propagating with a transverse component. With an effective path of $\hat{L} = 7a_0$ between tetrahedra #6 and #14 the wave speed relationship between the two tetrahedra is $\hat{c}/c_d = 0.57$. This value agrees with the wave speed value obtained with the FE model when accounting for the loss incurred on wave speed due to the contact stiffness.

We also considered the partially fused model case in the presence of friction ($\mu = 0.5$). Figure 19, shows the minimum (most compressive) principal stress for that model. Again, outside of the fused domain, tetrahedra #9 to #11, wave propagation is identical to that documented in Fig. 11. However, in the domain of the fused tetrahedra, the wave takes a direct path across tetrahedra #9 to #11 before resuming the transverse behavior. Applying the proposed path model in Fig. 17(b) but accounting for the fused tetrahedra, an effective path length of $\hat{L} = (3/2 + 11\sqrt{6}/8)a_0 \approx 8.87a_0$ between tetrahedra #6 and #14 is assumed and the resulting wave speed relationship between the two tetrahedra is $\hat{c}/c_d = 0.82$. The computed wave speed is $\hat{c}/c_d = 0.78$ which is in close agreement with the wave speed based on the proposed path after accounting for incurred loss due to contact stiffness.

With the idealized, linear, contact model, wave speeds are independent of the impact velocity. There is most certainly a need to understand the system behavior beyond the idealized contact contact interaction model. With the more realistic exponential contact (with $\mu = 0$), the model computations, on

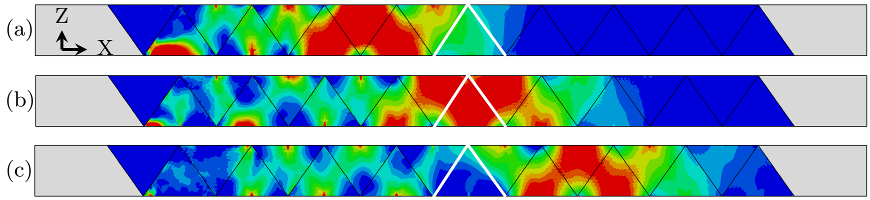

Fig. 19 Visualization of wave propagation through the partially fused tetrahedra assembly, linear contact model, $\mu = 0.5$, $V_0 = 1.0$ m/s, the white bars highlight the surfaces between tetrahedra #9 to #11 that have been fused together. Contour plots of the minimum (most compressive) principal stress, σ^P_{min} in the tetrahedra row cross section: (a) t =30 μs, (b) t = 40 μs, and (c) t =50 μs. Contour colors: blue ($\sigma^P_{min} > 0$ Pa) to red ($\sigma^P_{min} < 15 \times 10^6$ Pa).

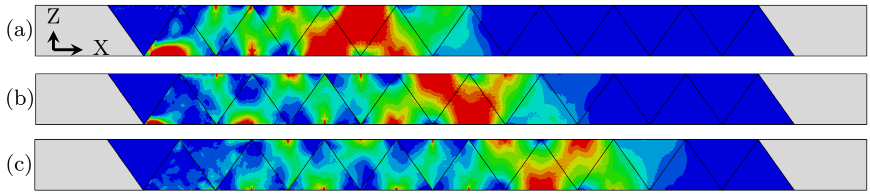

Fig. 20 Visualization of wave propagation through the tetrahedra assembly, exponential contact model for model (Exp-A), $\mu = 0.5$, $V_0 = 1.0$ m/s. Contour plots of the minimum (most compressive) principal stress, σ^P_{min} in the tetrahedra row cross section: (a) t =30 μs, (b) t = 40 μs, and (c) t =50 μs. Contour colors: blue ($\sigma^P_{min} > 0$ Pa) to red ($\sigma^P_{min} < 15 \times 10^6$ Pa).

the other hand, lead to a dependence of the wave speed on impact velocity. At the same time, no changes to the effective wave path relative to that for the idealized linear contact case is observed. It is therefore concluded that the nonlinear contact stiffness alone is responsible for the wave speed dependence on impact velocity.

While the combination of the exponential pressure overclosure contact model with friction was not explored as a parametric study, a computation with Exp-A with $\mu = 0.5$ at $V_0 = 1.0$ indicates that friction has a similar effect on both the linear and the exponential contact conditions. Figure 20 depicts the minimum (most compressive) principal stress for this case. The stress magnitude decreases across a time period of 20 μs and a residual stress field remains in the wake of the wave. A wave speed of $\hat{c}^\mu/c_d = 0.69$ was calculated and is higher than the $\mu = 0.0$ Exp-A model wave speed of $\hat{c}/c_d = 0.45$.

For the case of a linear contact model with $\mu = 0.0$, the width of the wave propagating through is constant with respect to reference input velocity (Fig. 5). This is not the case for models with friction (Fig. 10) or with nonlinear exponential contact (Fig. 13). Increasing the friction in the model leads to a narrowing of the wave width and a development of residual stress. The exponential models express the nonlinear stiffness in the wave shape during the rise of the wave. Figure 13 shows that rise occurs later in time in comparison to the data from the model with a linear contact interaction with $\mu = 0.0$ but decays over the same interval of time leading to a wave that is narrower than for the linear contact model with $\mu = 0.0$.

The development of contact is essential for the wave propagation. We extract contact pressure distributions and pitch angles for one sample tetrahedron (#9) to document the how wave propagation behavior is linked to contact. For linear contact interaction and $\mu = 0.0$, the model exhibits a pressure distribution that deviates from the static pressure distribution between tetrahedra, Fig. 8. The contact area and pressure distributions indicate that wave propagation is associated with a back-and-forth rotation of tetrahedra. Figure 9 exhibits such data for tetrahedron #9. In contrast, in a model with high friction, $\mu = 0.5$, the contact area and contact pressure distribution does not deviate from that under static loading. No rotation of the tetrahedron is present (Fig. 9). The more realistic, exponential pressure-overclosure, contact intersections, leads to an increase of the rotation, Fig. 16). In summary, the rotation of the tetrahedra, evidenced by the pitch angle evolution, does play a significant role in the wave propagation characteristics of the present system. Therefore, an effective quasi-static contact pressure model representing the force-displacement response of the tetrahedron-to-tetrahedron interaction alone cannot be used in the analysis of the present system.

In a chain of spheres, wave propagation is effectively unidirectional. Here, in the row of tetrahedra this is not the case, and the problem at least needs a 2D consideration of the guided wave configuration, Fig. 17. Friction is commonly not considered for chains of spheres but friction plays a significant role here as it determines the guided wave configuration, Fig. 17. The wave propagation through the row of tetrahedra is associated with a pitch evolution for the tetrahedra. Such considerations do not play a role in the row-of-spheres problem. When considering a system of spheres with properties (elastic, mass density and mass) equivalent to those of the tetrahedra in the present assembly, the effective wave speed along the chain of spheres is estimated to be less than $0.2c_d$ for the range of input velocities used ([5]), and the effective wave speed is dependent on the load magnitude. The effective wave speed for the idealized contact ranges from 0.47 to 0.81 c_d, depending on the friction condition. These values are upper bounds for real surfaces. Such real surfaces possess finite roughness are better described by the exponential pressure-overclosure models. Then, the effective wave speed is again dependent on the reference input velocity, Fig. 13(b).

5 Conclusion

When tetrahedra are assembled in topologically interlocked configuration, assembled structures, able to transfer mechanical loads are enabled in the in the absence of adhesion. Here, wave propagation in such a structure is documented. The key findings are as following:

- Wave propagation in the row of topologically interlocked tetrahedra occurs with a significant transverse component;
- The degree of the transverse component of wave motion depends on friction;
- Small rotations of building blocks lead to transients in the contact interactions and determine the degree of the transverse wave motion;
- In idealized, hard and linear contact interactions, wave speeds are independent of the impact speed, but are dependent on friction;
- Under realistic contact interactions, wave speeds are dependent of the impact speed and approach that of the idealized hard contact

The effective path models defined here provide predictions of the wave speeds obtained from detailed, full field finite element computations.

Appendix A Mesh Sensitivity

The mesh sensitivity of the model prediction was assessed by executing and evaluating computations with element edge lengths of $a_0/10$ (Seed10), $a_0/20$ (Seed20)and $a_0/40$ (Seed40). The of the integrated output section forces for all three mesh densities considered are presented in Fig. A1. For the case of the linear contact model with $\mu = 0.0$ and for $V_0 = 1.0$ m/s, Fig. A1(a) shows the models Seed20 and Seed40 lead to identical force histories while the results for model Seed10 depart slightly. The relative difference in computed wave speed of Seed10 to Seed20 is found as +4.9 %, and as −0.6 % between Seed40 and Seed20. The respective differences between peak forces are +7.8 % and −1.0 %. Considering a low impact velocity case, $V_0 = 0.1$ m/s, Fig. A1(b), similar differences are measured. The relative differences between Seed10 and Seed20 are found as +3.6 % and +8.9 % for wave speed and peak force respectively, while the relative differences between Seed40 and Seed20, −0.5 % and −1.2 %, respectively. Furthermore, the case of the linear contact model with $\mu = 0.5$, is considered. For $V_0 = 1.0$ m/s, from Fig. A1(c), the relative difference in wave speed between Seed10 and Seed20 is +0.8 % and the peak force difference is +10.7, while the respective relative differences between Seed40 and Seed20, are −0.3 % for wave speed and −1.9 % for the peak force. For $V_0 = 0.1$ m/s, from Fig. A1(d), the relative difference in wave speed between Seed10 and Seed20 is +1.2 % and the peak force difference is +11.6 %, while the respective relative differences between Seed40 and Seed20, are +0.1 % for wave speed and −2.1 % for the peak force.

The peak values of the integrated output section forces are more sensitive to the element size and that sensitivity increases as the wave traverses multiple unit building blocks. Overall, the change of the model predictions from models Seed20 to Seed40 is considered small enough such that using a element edge size of $a_0/20$ is acceptable for the present computations.

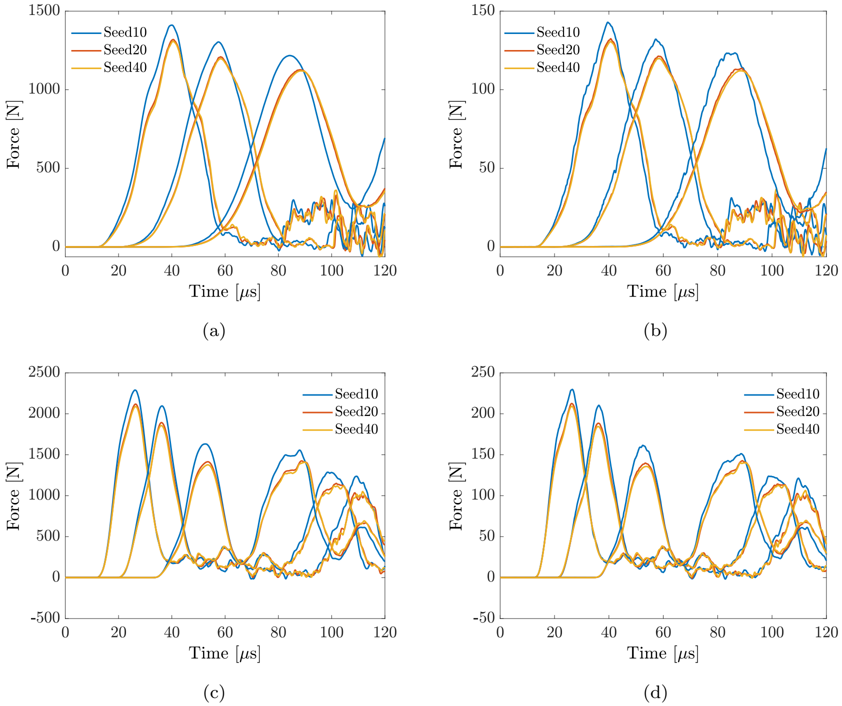

Fig. A1 Integrated output section force data of tetrahedra #6, #9, and #14 with different element edge sizes for: (a) $V_0 = 1.0$ m/s and $\mu = 0.0$, (b) $V_0 = 0.1$ m/s and $\mu = 0.0$, (c) $V_0 = 1.0$ m/s and $\mu = 0.5$, (d) $V_0 = 0.1$ m/s and $\mu = 0.5$. Seed10 corresponds to an element edge size of $a_0/10$, Seed20 corresponds to an element edge size of $a_0/20$, and Seed40 corresponds to an element edge size of $a_0/40$

References

[1] Nesterenko, V.F.: Dynamics of Heterogeneous Materials. Springer, New York (2012)

[2] Khatri, D., Ngo, D., Daraio, C.: Highly nonlinear solitary waves in chains of cylindrical particles. Granular Matter **14**, 63–69 (2012)

[3] Coste, C., Falcon, E., Fauve, S.: Solitary waves in a chain of beads under hertz contact. Physical Review E **56**, 6104–6117 (1997)

[4] Hua, T., Van Gorder, R.A.: Wave propagation and pattern formation in two-dimensional hexagonally-packed granular crystals under various configurations. Granular Matter **21**, 1–20 (2019)

[5] Ngo, D., Khatri, D., Daraio, C.: Highly nonlinear solitary wave in chains

of ellipsoidal particles. Physical Review E **84**, 026610 (2011)

[6] Job, S., Melo, F., Sokolow, A., Sen, S.: Solitary wave trains in granular chains: experiments, theory and simulations. Granular Matter **10**(1), 13–20 (2007)

[7] Nakagawa, M., Agui, J.H., Wu, D.T., Extramiana, D.V.: Impulse dispersion in a tapered granular chain. Granular Matter **4**(4), 167–174 (2003)

[8] Awasthi, S.P., Smith, K.J., Geubelle, P.H., Lambors, J.: Propagation of solitary waves in 2d granular media: A numerical study. Mechanics of Materials **54**, 100–112 (2012)

[9] Waymel, R.F., Wang, E., Awasthi, S.P., Geubelle, P.H., Lambors, J.: Propagation and dissipation of elasto-plastic stress waves in two dimensional ordered granular media. Journal of the Mechanics and Physics of Solids **120**, 117–131 (2018)

[10] Kim, E., Kim, Y.H.N., Yang, J.: Nonlinear stress wave propagation in 3d woodpile elastic metamaterials. International Journal of Solids and Structures **58**, 128–135 (2015)

[11] Dyskin, A.V., Estrin, Y., Kanel-Belov, A.J., Pasternak, E.: Topological interlocking of platonic solids: A way to new materials and structures. Philosophical Magazine Letters **83**, 197–203 (2003)

[12] Dyskin, A.V., Estrin, Y., Kanel-Belov, A.J., Pasternak, E.: A new concept in design of materials and structures: assemblies of interlocked tetrahedron-shaped elements. Scripta Materialia **44**, 2689–2694 (2001)

[13] Mirkhalaf, M., Zhou, T., Barthelat, F.: Simultaneous improvements of strength and toughness in topologically interlocked ceramics. Proceedings of the National Academy of Sciences **115**, 9128–9133 (2018)

[14] Williams, A., Siegmund, T.: Mechanics of topologically interlocked material systems under point load: Archimedean and laves tiling. International Journal of Mechanical Sciences **190**, 106016 (2021)

[15] Khandelwal, S., Siegmund, T., Cipra, R.J., Bolton, J.S.: Transverse loading of cellular topologically interlocked materials. International Journal of Solids and Structures **49**, 2394–2401 (2012)

[16] Short, M., Siegmund, T.: Scaling, growth, and size effects on the mechanical behavior of topologically interlocking material based on tetrahedral elements. Journal of Applied Mechanics **86**(2), 111007 (2019)

[17] Kim, D.Y., Siegmund, T.: Mechanics and design of topologically interlocked irregular quadrilateral tessellations. Materials & Design **212**, 110155 (2021)

[18] Leonard, A., Fraternali, F., Daraio, C.: Directional wave propagation in a highly nonlinear square packing of spheres. Experimental Mechanics **53**, 327–337 (2013)

[19] Siegmund, T., Barthelat, F., Cipra, R., Habtour, E., Riddick, J.: Manufacture and mechanics of topologically interlocked material assemblies. ASME Applied Mechanics Review **68**, 040803 (2016)

[20] Feng, Y., Siegmund, T., Habtour, E., Riddick, J.: Impact mechanics of topologically interlocked material assemblies. International Journal of Impact Engineering **75**, 140–149 (2015)

[21] Pasternak, E., Dyskin, A.V., Estrin, Y.: Deformations in transform faults with rotating crustal blocks. Pure and Applied Geophysics **163**, 2011–2030 (2006)

[22] Dyskin, A., Pasternak, E., Shufrin, I.: Structure of resonance and formation of stationary points in symmetrical chains of bilinear oscillators. Journal of Sound and Vibrations **333**, 6590–6606 (2014)

[23] He, J., Pasternak, E., Dyskin, A., Shufrin, I.: Rotational waves in fragmented and blocky geomaterials. EGU General Assembly Conference Abstracts, 9046 (2020)

[24] Torquato, S., Jiao, Y.: Exact constructions of a family of dense periodic packings of tetrahedra. Physical Review E **81**, 041310 (2010)

[25] Shi, X., Polycarpou, A.A.: Measurement and modeling of normal contact stiffness and contact at the meso scale. Journal of Vibration and Acoustics **127**, 52–60 (2005)